Tandem Cylinder Noise Predictions Using Lattice Boltzmann and Ffowcs Williams–Hawkings Methods

Guillaume A. Brès*
Exa Corporation, Brisbane, CA 94005

Michael Wessels† and Swen Noelting‡
Exa GmbH, Stuttgart, Germany

Numerical simulations of tandem cylinder flow are performed using Lattice-Boltzmann method, for comparison with experimental data. This case is considered an aeroacoustics benchmark as it incorporates the key flow features and interactions present in more complex realistic landing gears. The cylinders are separated in the streamwise direction by 3.7 diameters and the full span of 16 diameters is simulated, matching the experimental dimensions. For prediction of the radiated noise, a far-field noise solver based on the Ffowcs Williams–Hawkings equation is used. Results for a configuration with spanwise periodic boundary condition show excellent aggreement with the experimental surface and near-field data. Good correlation is also obtained for the far-field noise, but the peak levels are over estimated when the full length of the model span is used in the far-field solver. Similar over predictions are observed of the spanwise coherence and correlation of the surface pressure. Preliminary results for a configuration closely matching the experimental geometry (including the open jet and the solid end plates in the span) show an improved agreement for the spanwise correlation and the radiated noise.

Nomenclature

C_D	Drag coefficient
C_L	Drag coefficient
C_P	Coefficient of pressure
D	Cylinder diameter
L	Cylinder streamwise separation
P	Pressure
Re	Reynolds number
S	Cylinder span
U_0	Freestream velocity
u, v, w	Fluid velocity components
x, y, z	Streamwise, normal and spanwise directions
ρ	Density
θ	Azimutal angle

Subscript

0	Ambient quantity

Superscript

$\bar{}$	Time averaged quantity
$'$	Disturbance quantity (e.g., $\rho' = \rho - \rho_0$)

I. Introduction

Airframe noise has become one of the dominant noise sources during approach of modern transport aircraft due to recent improvements of other noise sources such as fan noise and jet noise. Due to the ever-increasing requirements for lower community noise the reduction of overall noise emissions from aircraft during take-off and landing is a critical requirement for future aircraft. With the recent reductions seen in engine noise, a significant portion of airframe noise is now the aerodynamic noise caused by the unsteady flow around the extended landing gear. However, prediction methods to estimate airframe noise in an early stage of the aircraft development process are still challenging, both for experiments and computations.

*Principal Aeroacoustics Engineer, Senior Member AIAA
†Validation Engineer
‡Managing Director, Exa GmbH, AIAA Member.

Recently, computational fluid dynamics tools based on the lattice-Boltzmann method have been applied successfully to aeroacoustics problems in both the aerospace[1,2] and automotive industries.[3–5] These methods offer significant advantages over traditional Navier-Stokes-based methods for the prediction of aeroacoustic phenomena. In particular these methods are inherently transient, have low numerical dissipation,[6,7] and are able to handle very complex geometries.

In the present study, the Lattice-Boltzmann method is applied to the simulation of a tandem cylinder configuration. This test case was proposed and designed as a benchmark test case for landing gear aeroacoustics as it incorporates the key flow features present in more complex realistic landing gears while being simple enough to allow extensive experimental investigations and to clearly identify and separate all relevant flow features. The tandem cylinder configuration is also one of the subjects of the AIAA Workshop on Benchmark problems for Airframe Noise Computations (BANC-1). A series of experiments were performed and both near-field aerodynamic data[8–11] and acoustic radiation measurements[10,12] are available.

The remainder of the paper is organized as follow. First, the experimental configurations and the numerical setup are reviewed and discussed in section II. Most of the numerical results presented in this paper correspond to a configuration with periodic boundary condition in the span, of dimension 16 diameters matching one of the experiments. Then, comparisons with the experimental surface and near-field data, as well as radiated noise levels are discussed in sections III and IV, respectively. The far-field noise prediction is preformed using an acoustic analogy solver based on the Ffowcs Williams–Hawkings (FW-H) equation.[13] The input to the FW-H solver is the time-dependent near-field on a surface mesh, both provided by LBM simulations. Finally, preliminary results for a configuration closely matching the experimental conditions (including the wind-tunnel open jet and the solid end plates in the span) are presented in section V.

II. Experimental setup and computational methods

A. BART and QFF experiment

Measurements of the unsteady flow around the tandem cylinders as well as aeroacoustic measurements both on the cylinder surface and in the far field were conducted in the NASA Basic Aerodynamics Research Tunnel (BART)[8–11] and the NASA Quiet Flow Facility (QFF).[10,12] Both wind-tunnels and experimental configurations are shown in figure 1.

(a) (b)

Figure 1. Tandem cylinder experimental setup: (a) BART facility; (b) QFF facility.

The BART facility is an open circuit wind tunnel with a test section area of 28" by 40" and a length of 120". Two cylinders were placed in the test section, each with a diameter of 1.75 inches. The flow Mach number was $M = 0.128$, which results in a Reynolds number of $1.66\ 10^5$. However, a boundary layer trip was used in the experiments to ensure fully turbulent flow on the cylinder. For the benchmark test selected, the identical cylinders are separated by a distance $L = 3.7D$ and the cylinder span is $S = 12.4D$. Experiments in the BART measured surface pressures (both steady and unsteady) using surface pressure transducers as well as unsteady and time-averaged flow field measurements using 2D Particle Image Velocimetry (PIV).

The QFF is an anechoic wind tunnel and provides microphone data to validate the radiated sound field.

Note that the tandem cylinders themselves are significantly smaller in this facility, $D = 0.05715$ m, and the cylinder span is $S = 16D$. The separation distance is still $L = 3.7D$. Three pole mounted microphones were used, each approximately 30D from the tandem cylinders and outside the shear layers formed by the open jet.

B. Lattice–Boltzmann methods

The CFD code PowerFLOW 4.2b based on the Lattice–Boltzmann method is used in this study. Unlike traditional methods solving the discretized Navier–Stokes equations on a computation grid, the LBM approach focuses on the mesoscopic scales via the discrete Boltzmann equation. That is, instead of studying the global behavior of a fluid, LBM tracks the statistical displacement of groups of particles and deducts the macroscopic scale behavior by evolving the particle distribution on a lattice.

The method is briefly reviewed here. The starting point is the distribution function F_i expressing the probability of presence of particles at position $\mathbf{x}$ and discrete velocity ξ_i at time t. The Lattice–Boltzmann equation is typically written in the following form:[14]

$$F_i(\mathbf{x} + \xi_i \Delta t, t + \Delta t) - F_i(\mathbf{x}, t) = \frac{\Delta t}{\tau} \left[F_i^{eq}(\mathbf{x}, t) - F_i(\mathbf{x}, t) \right]. \tag{1}$$

The left-hand side of equation (1) corresponds to the particle advection, while the right-hand side is the collision term, representing relaxation (i.e., interaction of the particles). The well-known BGK approximation[15] is used to compute the local equilibrium distribution function $F_i^{eq}(\mathbf{x}, t)$. The definition of the relaxation time τ is related to the kinematic viscosity and temperature by:

$$\tau = \frac{\nu}{T} + \frac{\Delta t}{2}. \tag{2}$$

The macroscopic quantities, density ρ and momentum density $\rho\mathbf{u}$, are determined directly from the distribution function F_i, using the moment summations:

$$\rho(\mathbf{x}, t) = \sum_i F_i(\mathbf{x}, t), \qquad \rho\mathbf{u}(\mathbf{x}, t) = \sum_i F_i(\mathbf{x}, t)\xi_i. \tag{3}$$

The full compressible viscous Navier–Stokes equations can be recovered from the Lattice–Boltzmann equation, using a multi-scale analysis,[16] for wavelengths $\lambda \gg \Delta x$ and frequencies $f \ll \Delta t$. The resulting equation of state is that of an ideal gas, in the form $P = \rho T$.

The numerical scheme is solved on a grid composed of cubic volumetric elements called voxels, and variable resolution (VR) is allowed, where the grid size changes by a factor of two for adjacent resolution regions. The local computational nature of LBM allows for excellent parallelization, and the method is well adapted to handle complex arbitrary geometries.

Together with the definition of F_i^{eq}, equations (1) and (2) constitute the LBM scheme used to perform direct numerical simulations (DNS). For high Reynolds number simulations, turbulence modeling is incorporated into the Lattice–Boltzmann equations by replacing the relaxation time by an effective turbulent relaxation time scale in equation (2). Additional details on the LBM numerical schemes, and the use of wall boundary conditions and turbulence modeling can be found in Refs. 17–20.

C. Numerical setup

In the current numerical simulation, the extent of the computation domain is $S = 16D$, with periodic boundary conditions in the spanwise direction. The other parameters and flow conditions matches the QFF experiment, namely $M = 0.128$ (corresponding to $U_0 = 44$ m/s), and $Re = U_0 D/\nu = 166\ 000$

A schematic of the numerical setup is presented in figure 2. The upstream cylinder is centered at (x/D,y/D) = $(0, 0)$ and the total size of the domain is approximately ($350D$, $280D$, $16D$). The upstream boundary condition is an inlet with uniform and constant streamwise velocity U_0, while the top, bottom, and downstream boundary conditions are pressure outlets ($P = P_0 = 100\ 000$ Pa). A large acoustic buffer zone with coarser resolution is implemented in the outer region to avoid any reflection and spurious waves. To duplicate the effect of the boundary layer trip used in the experiment, a surface roughness of 0.05 mm is used on the upstream cylinder, while the downstream cylinder has a standard no-slip boundary condition.

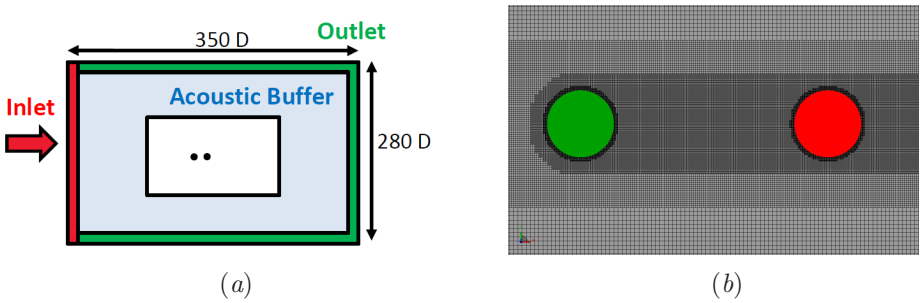

Figure 2. Simulation setup: a) schematic of the numerical domain (not to scale); (b) grid resolution.

As shown in Figure 2(b), resolution is primarily concentrated near the cylinders, with 128 cells per characteristic length D at the surface of both cylinders, leading to a finest cell size of 0.446 mm. This cell size is representative of the resolution typically used for practical landing gear noise prediction[21] with the current LBM solver. Particular care is also taken to have adequate resolution in the gap between the cylinders and in the wake, with a minimum of 64 cells per D covering the majority of these regions.

The initial condition is a uniform streamwise flow U_0 across the whole domain. The physical time step size is 7.35 10^{-7} s and the total simulated time is 0.5 s (i.e., about 680 000 time steps). The total number of voxels is approximately 66 million, while the fine equivalent number of voxels is 33 millions. The simulation was performed on 128 processors, for a total computational cost of about 25 kCPU hours.

III. Surface and near-field results

A. Temporal convergence and forces

The complete time history of lift and drag coefficients on both cylinders is shown in figure 3, to estimate temporal convergence. Note that the forces are nondimentionalized by $1/2\rho_0 U_0^2 A$, with $A = 16D^2$, to obtain the force coefficients. After the initial transient, the convergence is achieved for $t_0 \approx 0.1$ s. In the remainder of the paper, the mean and unsteady results presented correspond to the last 0.3-0.4 s of recorded data (i.e., more than 50 periods of the experimental shedding frequency). For most of the measurement, the sampling frequency is around 30 kHz and no less than 20 kHz.

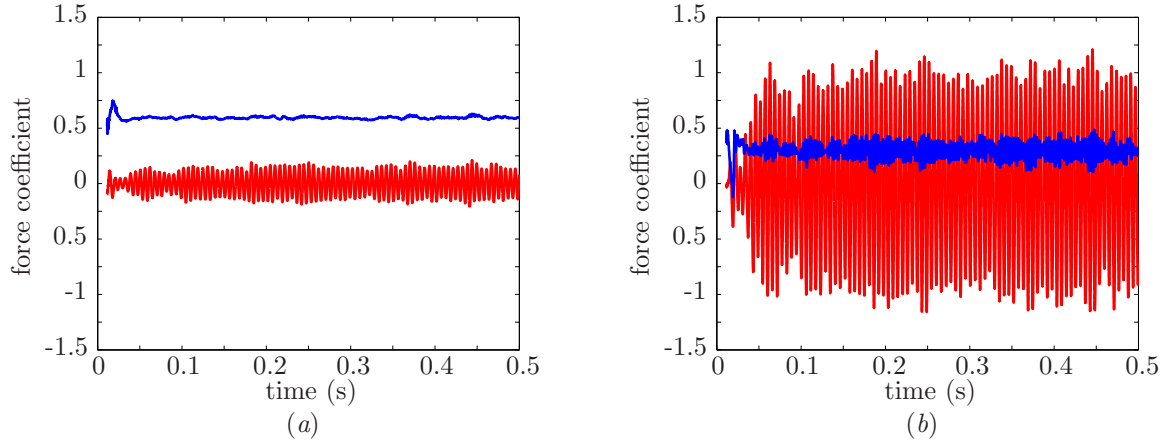

Figure 3. Time history of lift (———) and drag (———) coefficients: (a) upstream cylinder; (b) downstream cylinder.

From the data in figure 3, the mean drag coefficients can be estimated at $\bar{C}_D = 0.594$ for the upstream cylinder, and $\bar{C}_D = 0.294$ for the downstream cylinder. The primary shedding frequency is $f = 179$ Hz, in very good agreement with the experimental shedding frequency of 178-180 Hz.

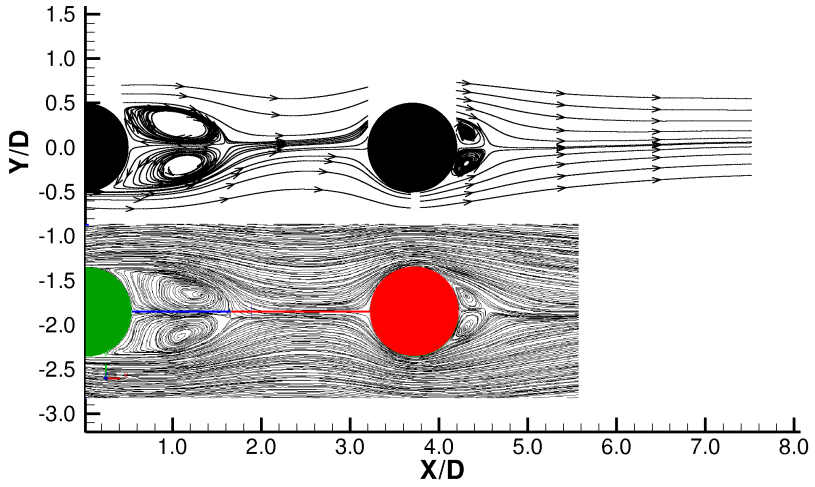

Figure 4. Streamlines in the midsection plane $z/D = 0$: PIV measurements (top); LBM simulation (bottom). The y-axis corresponds to the PIV data only.

B. Mean velocity field

Figure 4 shows the comparison between PIV measurements[22] and the mean flow structures between the cylinders from the LBM simulation, in the mid-section plane $z/D = 0$. The results indicate that both the shape and the length of the wakes are accurately predicted by the simulation.

The mean streamwise velocity (nondimensionalized by U_0) between the cylinders and after the downstream cylinder is shown in figure 5(a) and(b), respectively. Here, the numerical results are computed in the cross-section plane $y/D = 0$ and averaged in the spanwise direction. The agreement with the experimental measurement is excellent, in particular in the gap near the upstream cylinder (i.e., $0.5 < x/D < 2$) and after the downstream cylinder (i.e., $x/D > 4.2$). The velocity is slightly over predicted in the simulation for $2 < x/D < 3$, but within the uncertainty in the experimental and numerical data.

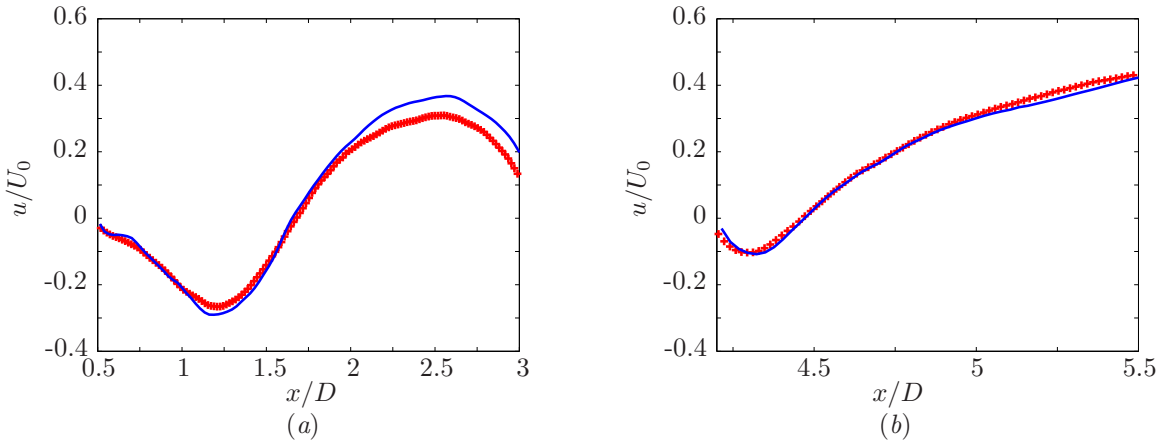

Figure 5. Mean streamwise velocity for BART experiment (+) and LBM simulation (———): (a) at $y/D = 0$ between the cylinders; (b) at $y/D = 0$ after the downstream cylinder.

C. Turbulent kinetic energy

The mean two-dimensional turbulent kinetic energy (nondimensionalized by U_0^2) is computed in the midsection plane $z/D = 0$ for comparison with PIV measurement. The results are presented between the cylinders

and after the downstream cylinder in figure 5(a) and(b). The simulation is on the top row and the experiment on bottom row, shown for the same scale and contour levels. Given the uncertainty that can be expected in both the experimental and numerical data for the estimation of the turbulent kinetic energy, the agreement is good. The shape and the overall levels are well capture in the simulation, with the peak levels slightly higher than in the experiment.

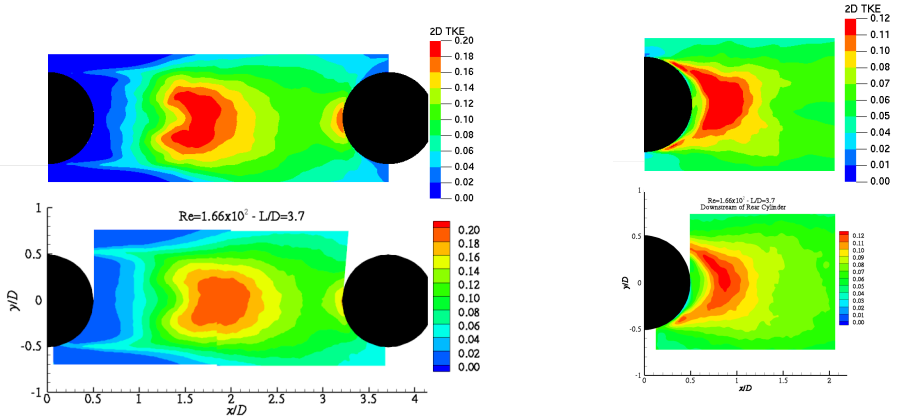

(a) (b)

Figure 6. Mean two-dimensional turbulent kinetic energy in the plane $z/D = 0$ from LBM simulation (top row) and BART experiment: (a) between the cylinder; (b) after the downstream cylinder.

D. Mean and unsteady surface pressure

A more quantitative comparison of mean flow structures, and in particular the location of the flow separation points on the front and rear cylinders, is possible using the static pressure measurement on the surface of the cylinders. The mean coefficient of pressure $C_P = (\bar{P} - P_0)/1/2\rho_0 U_0^2$ on the surface of both cylinders is presented in figure 7(a) and (b), as a function of the angle θ (measured from the upstream stagnation point). The simulation data is averaged in the spanwise direction. Again, there is an excellent agreement between the simulation and the experiment. As the LBM simulation matched the QFF setup in terms of dimensions and spanwise extent, an even better match is observed for the QFF data.

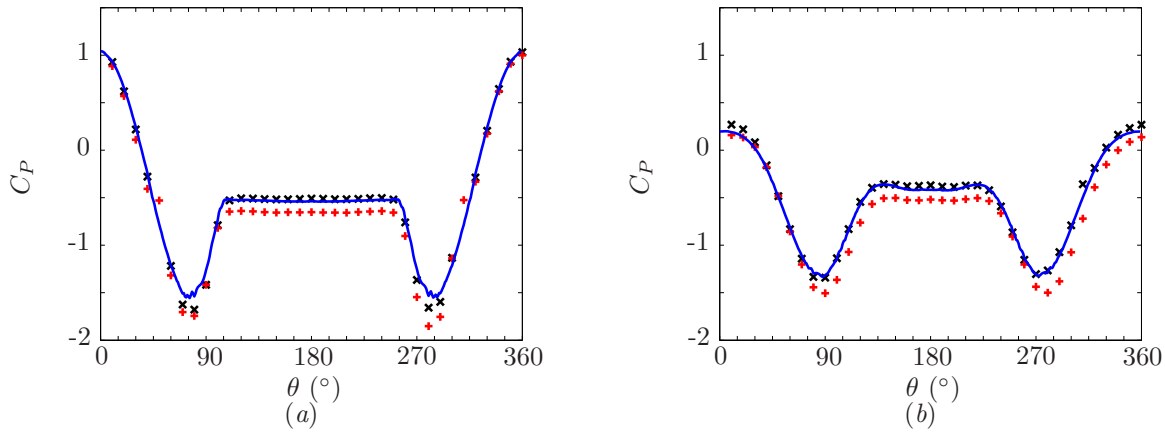

Figure 7. Mean coefficient of the surface pressure for BART (+) and QFF (×) experiments, and LBM simulation (———): (a) upstream cylinder; (b) downstream cylinder.

Similar agreement is obtained for the RMS of the coefficient of pressure in figure 10, in particular for the upstream cylinder. On the downstream cylinder, the shape of the curve is well captured in the simulation

but the RMS level are systematically higher, with up to 15% difference at the peak RMS. The increase in these fluctuation levels could potentially be attributed to the choice of the periodic boundary condition in the computation, as further discussed in section E.

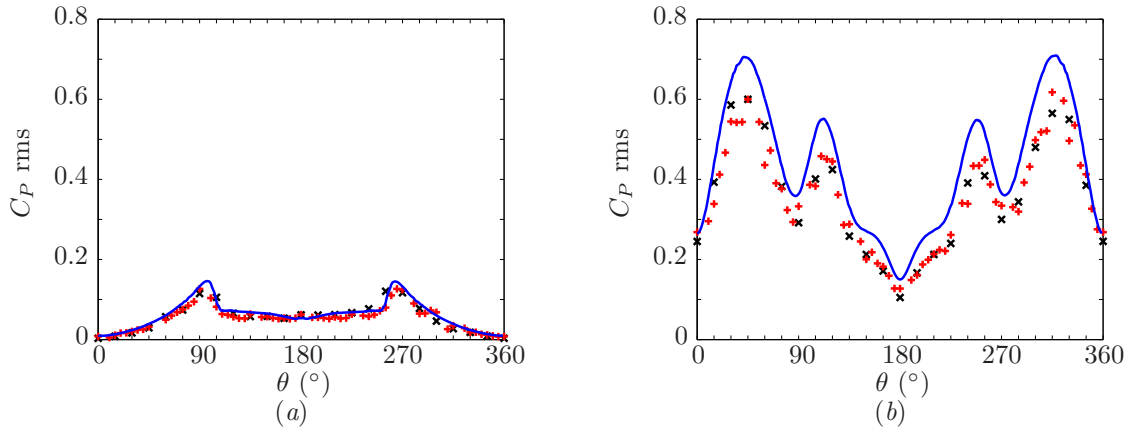

Figure 8. RMS of the coefficient of pressure for BART (+) and QFF (×) experiments, and LBM simulation (———): (*a*) downstream cylinder; (*b*) upstream cylinder.

Likewise, the pressure fluctuations on both cylinders are well predicted in the simulation, as shown in figure 4. On the downstream cylinder at $\theta = 45°$ (figure 9(*b*)), the agreement between the three data sets is nearly perfect. Even the small peaks at approximately 350 Hz, 550 Hz and 700 Hz are captured in the simulation. This measurement location corresponds to a region of strong interaction between the front wake and the downstream cylinder, leading to much higher dB levels than on the upstream cylinder. The primary shedding frequency in the simulation is $f \approx 179$ Hz, matching the measured shedding frequency of 178-180 Hz from the experiments.

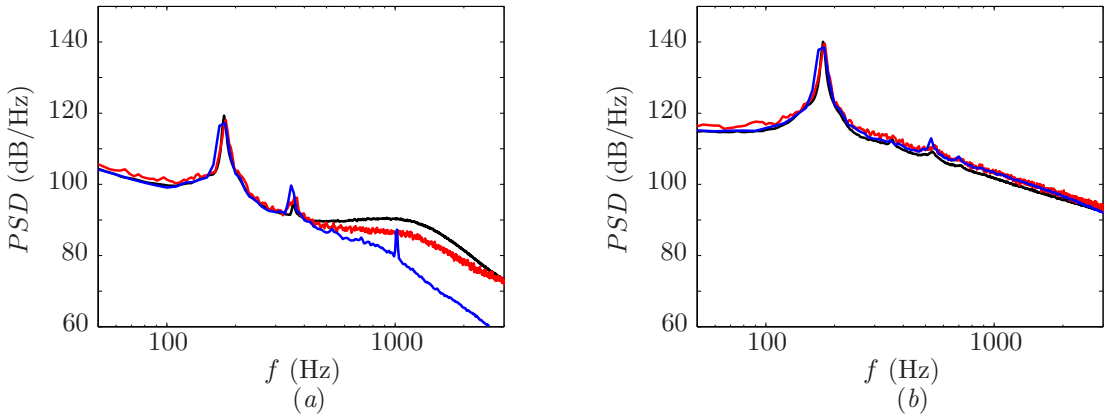

Figure 9. Surface pressure spectra for BART (———) and QFF (———) experiments, and LBM simulation (———): (*a*) upstream cylinder at $\theta = 135°$; (*b*) downstream cylinder at $\theta = 45°$.

On the upstream cylinder at $\theta = 135°$ (figure 9(*a*)), excellent agreement is again observed up to 500 Hz, with both the primary shedding frequency and the first harmonic accurately predicted. Above that frequency, there are significant differences between the three data sets. The pressure fluctuation levels in the experimental measurements tend to flatten out and remain constant around 90 dB (with the BART data about 3 to 5 dB lower) up to 1500 Hz, and then decay again at a constant rate. This particular shape of the spectra could potentially be caused by the boundary layer trip in the experiment. In contrast, there is no trip in the simulation and no change in slope in the spectra for the numerical results. The decay rate over these frequencies tends to match the value from the QFF data above 1500 Hz. Additionally, a peak of

approximately 8 dB is predicted around 1000 Hz, which is not observed in the experiments. This peak might be related to the surface roughness used in the simulation. Here, this particular measurement location is past the separation point of the upstream cylinder and experiences much smaller pressure fluctuations than the downstream cylinder.

Additional work and further analysis are required to investigate these differences and explain the presence of the peak at 1000 Hz in the simulation. Nevertheless, these results demonstrate that the mean and unsteady pressures on both cylinders are accurately predicted in the LBM computation. Since the differences occur at higher frequencies, and much smaller levels, it is not expected to significantly affect the radiated noise.

E. Spanwise coherence

Figure 10 shows the spanwise coherence of pressure at $\theta = 135°$ on both cylinders. The results from the numerical simulation (top row) are directly computed as a function of frequency and distance from the reference point (i.e., $z/D = 0$). For the experiments (bottom row), the coherence lengths were obtained for each frequency with a gaussian fit of the data.[23] Overall, the results show good agreement. As expected, the peak of coherence is observed at the primary shedding frequency on both cylinders. The peak at the first harmonic on the upstream cylinders is also well captured. However, the peak levels are overestimated in the simulation. A similar trend was observed in other numerical simulations with periodic spanwise boundary conditions,[10] for cylinders of shorter span (3D and 6D). However, a lower coherence is reported for the longer span of 18 diameters. Note that, unlike the results in Ref. 10, the CFD data is not averaged over all grid point combinations with the same spanwise spacing in the present work. The same over prediction is observed in the spanwise correlation of pressure at the same locations.

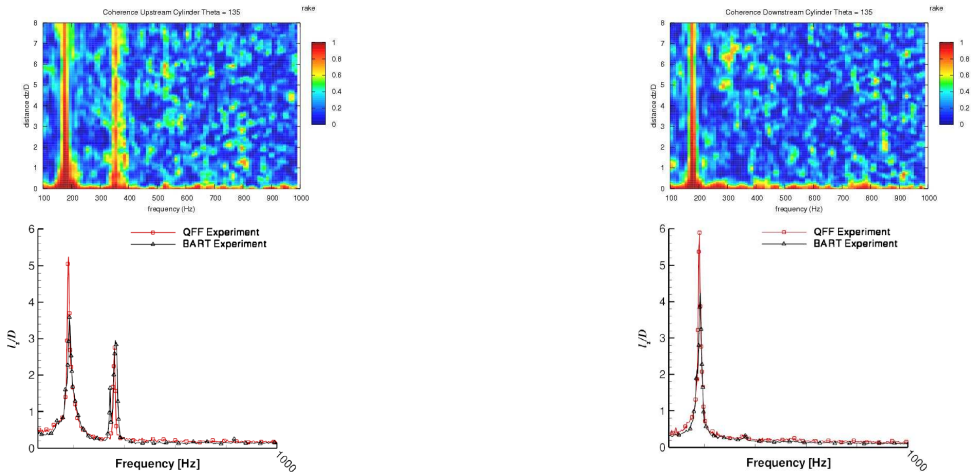

(a) (b)

Figure 10. Spanwise coherence of the surface pressure at $\theta = 135°$ from the LBM simulation (top) and from experiment[23] (bottom): (a) upstream cylinder; (b) downstream cylinder.

Additional analysis is needed to address these discrepancies, in particular on the effect of the spanwise periodic boundary condition and of the surface roughness. According to Zdravkovich,[24] surface roughness tends to enhance coherent shedding and spanwise uniformity by fixing the separation point. As a first step, simulations including the solid end walls in the spanwise direction are considered and are currently underway. Some preliminary results are discussed in section V.

IV. Far-field results

In the open-jet anechoic wind-tunnel, the radiated noise was measured at three microphones, within the mid-span plan above the cylinders. Microphone A is at $(-8.33D, 27.815D)$, microphone B at $(9.11D, 32.49D)$, and microphone C at $(26.55D, 27.815D)$. Shear-layer correction was not applied.

To efficiently predict the far-field noise at any location, an integrated post-processing module was developed.[25] This module uses an acoustic analogy solver based on the Ffowcs Williams–Hawkings (FW-H) equation[13] and can handle both moving (e.g. fly-over configuration) and stationary noise sources (e.g. wind-tunnel testing). The input to the FW-H solver is the time-dependent flow field on a surface mesh, both provided by CFD simulations with the LBM code. This surface mesh can be defined either as a solid (impenetrable) surface, or porous (permeable) data surface, to take into account nonlinearities in the vicinity of the source.

This case is representative of the *wind-tunnel* capability, and the acoustic analogy method is used to predict the noise at the same three microphone locations. For the results presented here, only the pressure fluctuations on the solid surface of both cylinders are used as input to the FW-H solver (i.e., solid surface formulation). In future work, additional CFD measurements in the cylinder near-field will be recorded to enable the use of the porous surface formulation.

The length of the time signal used as input for the far-field solver corresponds to the last 0.3 s of the simulation, which is more than 50 periods of the primary shedding frequency. The FW-H input measurement has a sampling rate of approximately 20 kHz, and contains about 1.5 million panels. The power spectra density (PSD) in dB/Hz (rel. to 20 10^{-6} Pa) is computed using hanning window (50% overlap), and samples of 10 Hz bandwidth.

Figures 11(a), (b) and (c) show the spectra of the radiated noise at the microphone A, B and C, respectively. Good agreement is obtained between the far-field solver predictions and the QFF measurements, for both the shape of the spectra and the overall levels. Similarly, the frequency of the tonal peak generated by the periodic shedding, as well as the first harmonics, is accurately predicted.

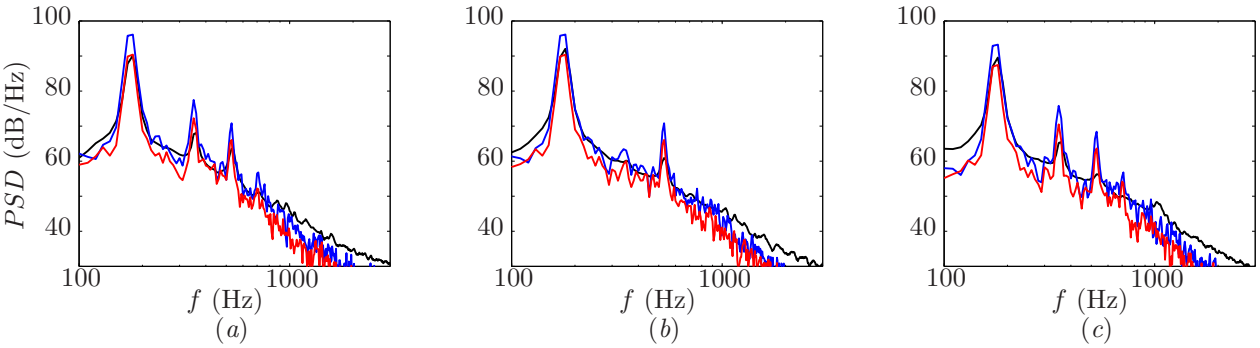

Figure 11. Power spectral density of the radiated noise for the QFF experiment (———), the FW-H solver for 16D span input (———), and 8D span input (———): (a) at microphone A; (b) at microphone B; (b) at microphone C.

However the predicted peak levels are systematically higher. This can be expected because of the periodic boundary conditions used in the simulation, compare to solid end walls in the experiments. In figure 11, the full span of 16D was used as input to the FW-H solver for the blue curves. In the BART and QFF experiments, the spanwise coherence at the shedding frequency is estimated around 4 to 6D. Similar results are reported for the spanwise correlation. Therefore, using only a reduced span of 8D as input to the FW-H solver, the predicted peak levels are reduced and now match the levels in the QFF experiments (red curve in figure 11). However, the overall levels tend to drop as well and the noise is slightly under predicted in this case.

V. Preliminary results for QFF simulations

Overall, the comparison of the far-field results show good agreement, but suggest that the solid walls present in the spanwise direction in the experiment should be included in the simulation, to obtain better correlation.

In order to address this issue and investigate installation effects, an additional configuration matching the QFF setup and geometry (including the open jet and the solid end plates in the span) is considered. The flow conditions, resolution, inlet/outlet boundary conditions and measurement parameters are unchanged. Figure

12 shows the geometry considered in the simulation, for comparison with the wind-tunnel configuration in figure 1(a). Here, the red crosses indicate the position of the measurement microphones A, B and C. Note that the exit manifold and deflector plate downstream of the jet are also included in the numerical setup. Additional details on the numerical setup and simulation will be presented in future publications.

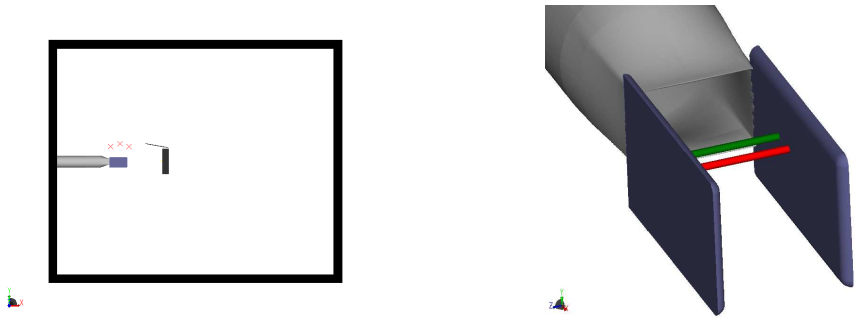

(a) (b)

Figure 12. QFF setup for the LBM simulation: (a) Computational domain; (b) Close up view of the open jet, tandem cylinders and end plates.

The simulation is initialized from a previous coarse run using a method of seeding, to allow the jet to develop and speed up the temporal convergence. Only 0.2 s of physical time is simulated at this stage, with the convergence approximately achieved again around 0.1 s. Therefore, the length of the time signal used as input to the FW-H solver corresponds to the last 0.1 s of the simulation, and the power spectra density, for both the simulation and the experiment, is now computed for samples of 20 Hz bandwidth. The new total number of voxels is 210 million. However, the fine equivalent number of voxels (i.e., the real measure of the true computational cost) is only increased to 41 million. The total computational cost is now about 12 kCPU hours for 0.2 s of data, which only a slight increase from the previous case.

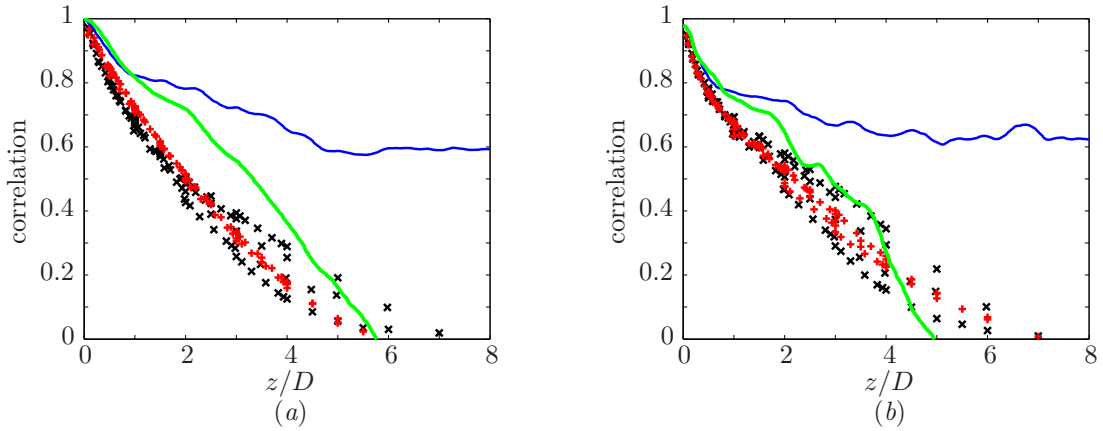

Figure 13. Spanwise correlation of the surface pressure at $\theta = 135°$ for the BART (+) and QFF (×) experiments, and LBM simulations with periodic span (———) and end plates (———): (a) upstream cylinder; (b) downstream cylinder. Only 0.1 s of data was available for the simulation with end plates.

Given the limited amount of data available at this stage, only a few representative quantities are analyzed and presented. The spanwise correlation is of particular interest here, to investigate the strong coherent shedding and spanwise uniformity observed in the previous numerical setup. Figure 13 shows the spanwise correlation of the surface pressure at $\theta = 135°$ on both cylinders, for the two experiments (BART and QFF), and the two LBM simulation (spanwise periodic and QFF setup). From figure 13, it is clear the inclusion of the end plate in the span significantly improves the comparison with the experiments. The trend is now similar and the agreement on the downstream cylinder is almost within the scattering of data. On the upstream cylinder, the spanwise correlation is still slightly over predicted in the simulation, potentially

because of the surface roughness.

The comparison between the experimental radiated noise and the new FW-H results (for the QFF setup) is shown in figure 14. Given the very short time signal used for the far-field prediction, these preliminary results are very encouraging. Here, the full span of the solid surface of both cylinders is again used as input to the FW-H solver. However, unlike the results with periodic boundary conditions in figure 11, the dB levels at the main peak frequency and the first harmonic are now well predicted. Likewise, the overall levels and shape of the spectra are well captured. A longer time signal and therefore better statistical averaging can be expected to improve the predictions in the low frequency and smooth out the dB levels. Further analysis, including comparisons with the experimental measurements for the mean and unsteady near-field, will be presented in future publications.

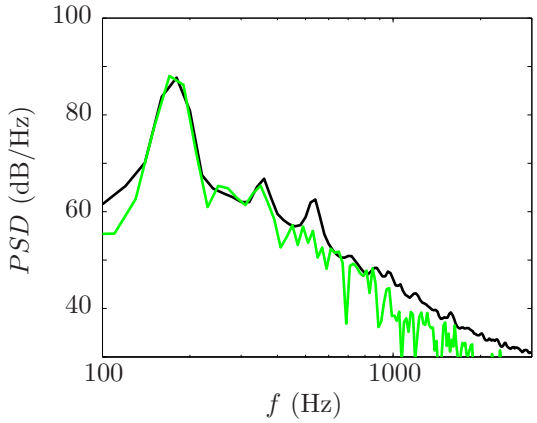

Figure 14. Power spectral density of the radiated noise at microphone A for the QFF experiment (———) and the FW-H solver (———) with the LBM simulation matching the QFF geometry. Only 0.1 s of data was available for the FW-H prediction.

VI. Conclusions

In this work, the Lattice-Boltzmann method is applied to the simulation of a tandem cylinder configuration with periodic boundary condition in the span. The numerical results are compared to experimental measurements from the BART and QFF wind-tunnel. The spanwise extent in the simulation is 16 diameters, matching the dimensions of the QFF setup. With the LBM solver, this large simulation is possible at reasonable computation cost (i.e., about 4 days on 256 processors for 0.5 s of data).

Overall, very good correlation is obtained between simulation and experiments for the surface data, for both mean and unsteady quantities. There is excellent agreement for the separation angles, the surface coefficient of pressure, and the lift and drag coefficients. The primary shedding frequency at $f = 178$ Hz is accurately predicted as well.

Good agreement is equally observed for the near-field data. The predicted streamlines and mean streamwise velocity between the cylinders and after the downstream cylinder match the experimental results. The correct trends for the two-dimensional turbulent kinetic energy in the midsection plane are also reported, even though this quantity can be challenging to measure for both methods.

For comparison with the measured radiated noise, a far-field noise prediction code based on the Ffowcs Williams–Hawkings (FW-H) equation is used. The input to the FW-H solver is the time-dependent flow field on a surface mesh, both provided by CFD simulations with the LBM code. For the current case, only the pressure fluctuations on the solid surface of both cylinders are used as input to the FW-H solver (i.e., solid surface formulation).

Good results are obtained using the FW-H solver for the same three microphone positions. The overall levels and the main peaks frequency (and harmonics) are well predicted. However the peak levels are higher. Likewise for the spanwise coherence and correlation: trends similar to the experiments are observed but larger values are predicted in the simulation. The spanwise periodic boundary conditions are anticipated to be the main cause of this enhanced coherent shedding and strong spanwise uniformity.

In order to address this issue and investigate installation effects, an additional configuration matching the QFF geometry (including the open jet and the solid end plates in the span) is considered. The preliminary results show that the inclusion of the spanwise end plate significantly improved the comparison with the experiments, for both the spanwise correlation and the far-field noise. Additional analysis and simulations are underway to confirm these findings.

Acknowledgments

The authors would like to thank David Lockard, Meelan Choudhari, Mehdi Khorrami, Dan Neuhart, and Florence Hutcheson, from NASA Langley Research Center, for providing the experimental data. The authors would also like to acknowledge the contributions of Rajani Satti, Leo Li and Rick Shock, from Exa Corporation, for the preliminary set of tandem cylinder simulations.

References

[1]Keating, A., Beedy, J., and Shock, R., "Lattice Boltzmann Simulations of the DLR-F4, DLR-F6 and Variants," AIAA Paper 2008-749, 2008.

[2]Keating, A., Dethioux, P., Satti, R., Noelting, S., Louis, J., Van de Ven, T., and Vieito, R., "Computational Aeroacoustics Validation and Analysis of a Nose Landing Gear," AIAA Paper 2009-3154, 2009.

[3]Ricot, D., Maillard, V., and Bailly, C., "Numerical Simulation of the Unsteady Flow Past a Cavity and Application to Sunroof Buffeting," AIAA Paper 2001-2112, 2001.

[4]Crouse, B., Senthooran, S., Freed, D., Balasubramanian, G., Gleason, M., Puskarz, M., Lew, P., and Mongeau, L., "Experimental and Numerical Investigation of a Flow Induced Cavity Resonance with Application to Automobile Buffeting," AIAA Paper 2006-2494, 2006.

[5]Adam, J.-L., Ricot, D., Dubief, F., and Guy, C., "Aeroacoustic simulation of automobile ventilation outlets," JASA vol. 123, issue 5, p. 3250, 2008.

[6]Marié, S., Ricot, D., and Sagaut, P., "Comparison between lattice Boltzmann method and Navier–Stokes high order schemes for computational aeroacoustics," *J. Comput. Phys.*, Vol. 228, 2009, pp. 1056–1070.

[7]Brès, G. A., Pérot, F., and Freed, D., "Properties of the Lattice–Boltzmann Method for Acoustics," AIAA Paper 2009-3395, 2009.

[8]Jenkins, L. N., Khorrami, M. R., Choudhari, M. M., and McGinley, C. B., "Characterization of unsteady flow structures around tandem cylinders for component interaction studies in airframe noise," AIAA paper 2005-2812, 2005.

[9]Jenkins, L. N., Neuhart, D. H., McGinley, C. B., Choudhari, M. M., and Khorrami, M. R., "Measurements of unsteady wake interference between tandem cylinders," AIAA paper 2006-3202, 2006.

[10]Lockard, D. P., Khorrami, M. R., Choudhari, M. M., Hutcheson, F. V., Brooks, T. F., and Stead, D. J., "Tandem cylinder noise predictions," AIAA paper 2007-3450, 2007.

[11]Neuhart, D. H., Jenkins, L. N., Choudhari, M. M., and Khorrami, M. R., "Measurements of the flowfield interaction between tandem cylinders," AIAA paper 2009-3275, 2009.

[12]Hutcheson, F. V. and Brooks, T. F., "Noise radiation from single and multiple rod configurations," AIAA paper 2006-2629, 2006.

[13]Ffowcs Williams, J. E. and Hawkings, D. L., "Sound generation by turbulence and surfaces in arbitrary motion," *Proc. R. Soc. Lond. A*, Vol. 264, 1969, pp. 321–342.

[14]Wolf-Gladrow, D., *Lattice-Gas Cellular Automata and Lattice Boltzmann Models*, Springler Verlag, Germany, 2000.

[15]Bhatnagar, P., Gross, E., and Krook, M., "A model for collision progresses in gases. I. small amplitude processes in charged and neutral one-component system," *Phys. Rev.*, Vol. 94(3), 1954, pp. 511–525.

[16]Chapman, S. and Cowling, T., *The Mathematical Theory of Non-Uniform Gases*, Cambridge University Press, 1990.

[17]Chen, H., Teixeira, C., and Molvig, K., "Realization of Fluid Boundary Conditions via Discrete Boltzmann Dynamics," *Intl. J. Mod. phys. C*, Vol. 9(8), 1998, pp. 1281.

[18]Chen, H., "Volumetric Formulation of the Lattice Boltzmann Method for Fluid Dynamics: Basic Concept," *Phys. Rev. E*, Vol. 58, 1998, pp. 3955–3963.

[19]Chen, S. and Doolen, G., "Lattice Boltzmann Method for Fluid Flows," *Ann. Rev. Fluid Mech.*, Vol. 30, 1998, pp. 329–364.

[20]Chen, H., Orszag, S., Staroselsky, I., and Succi, S., "Expanded Analogy between Boltzmann Kinetic Theory of Fluid and Turbulence," *J. Fluid Mech.*, Vol. 519, 2004, pp. 307–314.

[21]Noelting, S., Brès, G. A., Dethioux, P., Van de Ven, T., and Vieito, R., "A Hybrid Lattice-Boltzmann/FH-W Method to Predict Sources and Propagation of Landing Gear Noise," AIAA Paper 2010-3976, 2010.

[22]Khorrami, M. R., Choudhari, M. M., Lockard, D. P., Jenkins, L. N., and McGinley, C. B., "Unsteady Flowfield Around Tandem Cylinders as Prototype Component Interaction in Airframe Noise," *AIAA J.*, Vol. 45(8), 2007, pp. 1930–1941.

[23]Lockard, D. P., "Tandem cylinder benchmark problem," AIAA Workshop on Benchmark problems for Airframe Noise Computations (BANC-1), 2007.

[24]Zdravkovich, M. M., *Flow Around Circular Cylinders Volume 1*, Oxford University Press, 1977.

[25]Brès, G. A., Pérot, F., and Freed, D., "A Ffowcs Williams–Hawkings Solver for Lattice-Boltzmann based Computational Aeroacoustics," AIAA Paper 2010-3711, 2010.